The Drag Instability in a 1D Isothermal C-shock

Pin-Gao Gu[1] and Che-Yu Chen[2]
[1] Institute of Astronomy & Astrophysics, Academia Sinica, Taipei 10617, Taiwan; gu@asiaa.sinica.edu.tw
[2] Department of Astronomy, University of Virginia, Charlottesville, VA 22904, USA
Received 2020 March 31; revised 2020 May 28; accepted 2020 June 23; published 2020 July 24

Abstract

We investigate whether the drag instability, proposed by Gu et al., occurs in a one-dimensional (1D) C-shock. The 1D background model proposed by Chen & Ostriker for a steady isothermal C-shock is adopted, and a 1D isothermal linear analysis is performed. We confirm the postulation of Gu et al. that the drift velocity between ions and neutrals is sufficiently high within a C-shock to allow for the drag instability. We also study the underlying physics of the decaying modes in the shock and postshock regions. The drag instability is an overstability phenomenon associated with an exponentially growing mode of a propagating wave. We find that the growing wave mode can only propagate downstream within the shock and subsequently decay in the postshock region. The maximum total growth for such an unstable wave before it is damped is estimated in typical environments of star-forming clouds, which is approximately 10–30 times larger than the initial perturbation at the modest shock velocities and can be significantly enhanced several hundred times for a stronger C-shock with a larger width.

Unified Astronomy Thesaurus concepts: Interstellar clouds (834); Shocks (2086); Plasma astrophysics (1261); Star forming regions (1565); Molecular clouds (1072); Interstellar magnetic fields (845)

1. Introduction

Stars form within molecular clouds (Shu et al. 1987), which are the densest subregions of the interstellar medium (ISM). While the galactic star formation efficiency is heavily regulated by thermal and dynamic feedback from young stars (see, e.g., Ostriker et al. 2010), it is widely recognized that the interstellar magnetic field plays a critical role in modifying the star formation process locally within individual clouds (McKee & Ostriker 2007; Crutcher 2012). However, the gas in these cold molecular clouds and their substructures is generally weakly ionized (see, e.g., Tielens 2005; Dalgarno 2006), and the actual ability of magnetic fields to affect star formation thus relies on the collisional coupling between neutrals and ions (Mouschovias 1979).

With the existence of a spatial gradient of the field lines to exert a Lorentz force on the ions, the ions can drift relative to the neutrals. As the result, ambipolar diffusion occurs when the drag force (proportional to the ion–neutral collision rate; Spitzer 1956) is balanced by the Lorentz force, leading to the diffusion of the magnetic fields from the neutrals (Shu 1992). This allows the redistribution of neutral gas relative to the magnetic flux (Mestel & Spitzer 1956). Ambipolar diffusion has been considered as the main mechanism for several processes during star formation, including the collapse of magnetically supported overdense subregions within the molecular clouds (Mouschovias 1978; Nakano & Nakamura 1978; Lizano & Shu 1989; Fiedler & Mouschovias 1992, 1993; Oishi & Mac Low 2006; Li et al. 2008), enhanced angular momentum transport (compared to that in the magnetic braking catastrophe) during protostellar disk formation (Mellon & Li 2009; Dapp et al. 2012; Hennebelle et al. 2016; Masson et al. 2016; Vaytet et al. 2018; Lam et al. 2019), and the development of substructures in protoplanetary disks (Bai & Stone 2011; Lesur et al. 2014; Gressel et al. 2015; Riols & Lesur 2018; Suriano et al. 2018, 2019).

Alternatively, Gu et al. (2004; hereafter GLV) studied the stability of ambipolar drift in a weakly ionized fluid. GLV

simplified the problem by representing it as that of a 1D drift flow threaded with perpendicular magnetic fields. GLV discovered a local overstable mode provided that the ion–neutral drift velocity $v_d \equiv |v_{ion} - v_{neutral}|$ is as high as the Alfvén velocity of the bulk fluid ($V_A \equiv B/\sqrt{4\pi\rho}$), and if the ionization equilibrium can be sustained. Although a high drift velocity arises from a strong Lorentz force, the instability in its simplest form is not related to any magnetosonic or acoustic modes, but is caused solely by the pronounced drag force induced by the high drift velocity. Consequently, GLV named the instability "drag instability." We use this same terminology to refer to the overstability in this paper.

In general, the drag caused by the drift motion between two fluids alone (i.e., independent of Alfvén, magnetosonic, or acoustic modes) can provide free energy to facilitate a fluid instability under favorable conditions. A notable example of this phenomenon is the streaming instability caused by the dust-gas drift motion in a protoplanetary disk (e.g., Youdin & Goodman 2005). Because the drag instability requires a high ambipolar drift velocity, GLV postulated that the instability occurs in regions where magnetic fields are highly stressed, including interstellar shock systems and/or collapsing proto-stellar cores. While there is evidence that the ion–neutral drift velocity within collapsing protostellar envelopes could be as high as the freefall velocity ($\sim 1\,\mathrm{km\,s^{-1}}$; see, e.g., Yen et al. 2018; Lam et al. 2019), in this study we focus on interstellar shock systems with efficient ambipolar diffusion to investigate whether the drag instability can take place during the compression that initiates star formation.

In the ISM, stressed magnetic fields may occur due to shock compression triggered by clump–clump collision or supersonic, turbulent gas flows within giant molecular clouds (e.g., Mestel & Spitzer 1956; Draine & McKee 1993; Ostriker et al. 1999; Ballesteros-Paredes et al. 2007; Federrath et al. 2011; Li et al. 2014). While jump-type (J-type) shocks exhibit sharp super-sonic (or super-Alfvénic for magnetized shocks) discontinuities in physical properties, in the case of nonideal magnetohydro-dynamics (MHD), continuous-type (C-type) shocks manifest as

a smooth transition between the pre-and postshock regions due to the ambipolar drift between ions and neutrals. Specifically, when the ion–neutral drift velocity is lower than the Alfvén speed of the ions, the Alfvén speed of the ions can propagate the shock signal upstream, thereby compressing the ions and magnetic fields and subsequently dragging and compressing the neutrals. This process smoothens out the sharp transition and results in a width of the continuous shock profile between the pre- and postshock regions (Draine 1980; Draine & McKee 1993).

In the cold molecular clouds and their substructures (temperature ∼10 K; see, e.g., Fukui & Kawamura 2010), the ionization rate by cosmic rays is relatively low ($\xi_{CR} \sim 10^{-17}\,\mathrm{s}^{-1}$; see, e.g., Draine et al. 1983; Indriolo & McCall 2012). The star-forming gas is therefore mainly composed of the neutrals with only a small abundance of ions, with typical ionization fraction $\lesssim 10^{-6}$ (Tielens 2005; Dalgarno 2006). Such weakly ionized gas, when compressed by supersonic turbulence, provides the favored conditions for large ion–neutral drifts and C-type shocks. There have been various observational efforts to probe such features in turbulent molecular clouds (e.g., Li & Houde 2008; Hezareh et al. 2010, 2014; Xu & Li 2016; Tang et al. 2018), although most of these observations are indirect measurements and highly dependent on the adopted dynamical and chemical models (e.g., Flower & Pineau Des Forêts 1998, 2010; Gusdorf et al. 2008; Lehmann & Wardle 2016; Valdivia et al. 2017). Theoretically, previous studies have investigated in detail the formation as well as the physical and chemical properties of C-shocks (e.g., Wardle 1990; Mac Low et al. 1995; Pineau des Forets et al. 1997; Smith & Mac Low 1997; Guillet et al. 2011). In particular, Chen & Ostriker 2012 (hereafter CO12) studied the 1D isothermal C-shock along the drift direction with a transverse magnetic field. They analytically derived the 1D structure of a C-shock, thereby providing an appropriate and convenient background state for the 1D linear analysis of the drag instability proposed in GLV.

We note that while we focus on C-shock instability in this study, the drag instability could exist in other systems with enhanced drift velocities (see GLV). Moreover, the drag instability differs from the Wardle instability, originally proposed for C-shock systems in Wardle (1990), which is analogous to the Park instability, with the ion–neutral drag playing a role of gravity to collect matters in the magnetic "valley." The Wardle instability therefore requires the wiggle of 2D or 3D field lines and exists as a more global mode along the shock direction. In contrast, the drag instability can exist in a 1D flow and is a local effect.

Furthermore, among all previous investigations of the 1D C-shock structure (e.g., Smith & Mac Low 1997; Chieze et al. 1998; Ciolek & Roberge 2002; van Loo et al. 2009; Ashmore et al. 2010), only the simplified scenario discussed in CO12 (isothermal gas with ionization-recombination equilibrium) provides a suitable condition for the drag instability to occur. We further note that the drag instability differs from the fragmentation instability (Zweibel 1998), which requires the system to be near marginal dynamical stability so that the release of energy through diffusion of the magnetic field could lead to runaway contraction of an initially overdense region. The drag instability, on the other hand, does not require hydrostatic equilibrium, and the ultimate source of energy comes from the stressed magnetic fields.

The outline of the paper is as follows. In Section 2 we first review the steady-state C-shock solution of CO12 and the linear theory of GLV. By considering a fiducial C-shock model as the background state (Section 2.2), we present the dispersion relation for the drag instability and the other dispersion relations in the postshock region (Section 2.3). The exact solutions of the eigenvalues and eigenmodes are obtained by solving the linearized equations and are analyzed using the dispersion relations (Section 2.4). In Section 3 we present the maximum total growth (MTG) obtained for the unstable mode under the drag instability within a C-shock using the fiducial model and other models with different preshock conditions. We discuss the connection between this analytic work and previous numerical time-dependent simulations in Section 4. Finally, the results of this study are summarized in Section 5.

2. Linear Analysis: WKBJ Analysis

In general, the dynamical evolution of ions and neutrals is governed by their individual continuity and momentum equations, in addition to the collisional drag force, cosmic-ray ionization, ion–electron recombination in the gas phase, and the induction equation for ions (e.g., Draine 1980; Shu 1992; Chen & Ostriker 2012). The equations are

$$\frac{\partial \rho_n}{\partial t} + \nabla \cdot (\rho_n \boldsymbol{v_n}) = 0, \tag{1}$$

$$\frac{\partial \rho_i}{\partial t} + \nabla \cdot (\rho_i \boldsymbol{v_i}) = -\beta \rho_i^2 + \xi_{CR} \rho_n, \tag{2}$$

$$\rho_n \left[\frac{\partial \boldsymbol{v_n}}{\partial t} + (\boldsymbol{v_n} \cdot \nabla) \boldsymbol{v_n} \right] + \nabla p_n = \boldsymbol{f_d}, \tag{3}$$

$$\rho_i \left[\frac{\partial \boldsymbol{v_i}}{\partial t} + (\boldsymbol{v_i} \cdot \nabla) \boldsymbol{v_i} \right] + \nabla p_i - \frac{1}{4\pi} (\nabla \times \boldsymbol{B}) \times \boldsymbol{B} = -\boldsymbol{f_d}, \tag{4}$$

$$\frac{\partial \boldsymbol{B}}{\partial t} + \nabla \times (\boldsymbol{B} \times \boldsymbol{v_i}) = 0, \tag{5}$$

where $\boldsymbol{v}$ is the velocity, ρ is the density, $\boldsymbol{B}$ is the magnetic field, $p = \rho c_s^2$ is the gas pressure when the isothermal sound speed c_s is $0.2\,\mathrm{km\,s^{-1}}$ at a temperature ∼10 K, and the subscripts i and n denote the ion and neutral species, respectively. Note that the neutrals and ions are coupled by the collisional drag force $\boldsymbol{f_d} \equiv \gamma \rho_i \rho_n \boldsymbol{v_d} = \gamma \rho_i \rho_n (\boldsymbol{v_i} - \boldsymbol{v_n})$, where $\gamma \approx 3.5 \times 10^{13}\,\mathrm{cm^3\,s^{-1}\,g^{-1}}$ is the drag force coefficient (Draine et al. 1983). The evolution of ion number density is controlled by the cosmic-ray ionization rate ξ_{CR} and the ion recombination in the gas phase β (see, e.g., CO12).

2.1. Background States and Linearized Equations

Following the simplified scenario discussed in Chen & Ostriker (2012) that the magnetic field is perpendicular to the gas flow toward the $+x$ direction through the shock, the equilibrium equations in this 1D C-shock system are given by

$$V_n \frac{d\rho_n}{dx} = -\rho_n \frac{dV_n}{dx}, \tag{6}$$

$$V_n \frac{dV_n}{dx} = \gamma \rho_i V_d - \frac{c_s^2}{\rho_n} \frac{d\rho_n}{dx}, \tag{7}$$

$$\beta \rho_i^2 = \xi_{CR} \rho_n, \tag{8}$$

$$\gamma \rho_n V_d = -V_{A,i}^2 \frac{d \ln B}{dx}, \qquad (9)$$

$$V_i \frac{dB}{dx} = -B \frac{dV_i}{dx}. \qquad (10)$$

$$C = \begin{bmatrix} -\mathrm{i}kV_i - 2\beta\rho_i & -\mathrm{i}k\rho_i & 0 & \xi_{\mathrm{CR}} & 0 \\ -\mathrm{i}k\frac{c_s^2}{\rho_i} & -\mathrm{i}kV_i - \gamma\rho_n & -\mathrm{i}k\frac{V_{A,i}^2}{B} & -\gamma V_d & \gamma\rho_n \\ 0 & -\mathrm{i}kB & -\mathrm{i}kV_i & 0 & 0 \\ 0 & 0 & 0 & -\mathrm{i}kV_n & -\mathrm{i}k\rho_n \\ \gamma V_d & \gamma\rho_i & 0 & -\mathrm{i}k\frac{c_s^2}{\rho_n} & -\mathrm{i}kV_n - \gamma\rho_i \end{bmatrix}. \qquad (15)$$

In the above equilibrium equations, we consider the strong-coupling approximation under which the ion–neutral drag is balanced by the magnetic pressure gradient for the ions; i.e., $\gamma\rho_n L_B V_d = V_{A,i}^2$ where $L_B \equiv (-d\ln B/dx)^{-1}$. In addition, the equilibrium between cosmic ionization and recombination is assumed; namely, $\beta\rho_i^2 = \xi_{\mathrm{CR}}\rho_n$ (see CO12 for justifications of this choice). We note that these equilibrium states are consistent with the background states considered by GLV.

By subjecting the equilibrium equations to the zero-gradient boundary conditions ($d/dx = 0$) far upstream and downstream (i.e., no structures in the steady pre- and postshock regions), CO12 derived the 1D structure equation of a C-shock as follows (here and throughout this paper, we use the subscript 0 to denote a physical quantity in the preshock region):

$$\frac{dr_B}{dx} = -\frac{\gamma\rho_{i,0}}{v_0} \mathcal{M}_A^2 \frac{r_n^{3/2}}{r_B}\left(\frac{1}{r_B} - \frac{1}{r_n}\right), \qquad (11)$$

where the field compression ratio is $r_B \equiv B/B_0 = V_{i,0}/V_i$, the neutral compression ratio is $r_n \equiv \rho_n/\rho_{n,0} = V_{n,0}/V_n$, and the Alfvén Mach number $\mathcal{M}_A$ for the shock velocity v_0 is defined as $v_0/V_{A,n,0}$. Note that r_n can be written as a function of r_B:

$$\begin{aligned} r_n = [1 + 2\mathcal{M}_A^2 + \beta_{\mathrm{plasma}} - r_B^2 \\ - \sqrt{[1 + 2\mathcal{M}_A^2 + \beta_{\mathrm{plasma}} - r_B^2]^2 - 8\beta_{\mathrm{plasma}}\mathcal{M}_A^2}\,]/2\beta_{\mathrm{plasma}}, \end{aligned} \qquad (12)$$

with the plasma beta value $\beta_{\mathrm{plasma}} \equiv 8\pi\rho_0 c_s^2 / B_0^2$. By placing the shock front at $x = 0$, the physical quantities along the C-shock can be obtained by integrating the ordinary different equation (Equation (11)) backward from far downstream, where

$$\begin{aligned} r_B = r_n = 4\mathcal{M}_A^2/[1 + \beta_{\mathrm{plasma}} \\ + [(1 + \beta_{\mathrm{plamsa}})^2 + 8\mathcal{M}_A^2]^{1/2}] \end{aligned} \qquad (13)$$

to far upstream. In this setup of the problem, the background drift velocity $V_d = V_i - V_n < 0$ inside the C-shock (i.e., within the smooth shock transition).

We now consider the perturbations $U(\omega, k) \equiv (\delta\rho_i, \delta v_i, \delta B, \delta\rho_n, \delta v_n)^T$ multiplied by $\exp[\mathrm{i}(kx + \omega t)]$ under the Wentzel–Kramers–Brillouin–Jeffreys (WKBJ) approximation. By substituting these perturbations and the background states into the Equations (1)–(5), the following linearized equations are obtained (GLV):

$$CU = \mathrm{i}\omega U, \qquad (14)$$

where

Hence, we can solve the above equations as an eigenvalue problem with ω being the eigenvalue and U being the eigenfunctions. The goal is to identify a maximum-growth mode associated with the drag instability within the C-shock.

2.2. Fiducial Model

We adopt the 1D steady-state C-shock profile shown in Figure 3 of CO12 as the background state (in the shock frame) of our fiducial model. The preshock parameters are $n_0 = 500 \, \mathrm{cm}^{-3}$ (neutral number density), $V_{i,0} = V_{n,0} = v_0 = 5 \, \mathrm{km\,s}^{-1}$ (shock velocity), $B_0 = 10 \, \mu\mathrm{G}$, and ionization fraction coefficient $\chi_{i0} = 10$. Here, the parameter χ_{i0} is defined in the expression $n_i = 10^{-6}\chi_{i0} n_n^{1/2}$ of CO12 assuming ionization-recombination equilibrium, and is therefore given by $\chi_{i0} \equiv 10^6 \sqrt{\xi_{\mathrm{CR}}(m_n/m_i)/(\beta m_i)}$. We thus adopted $\beta \approx 10^{-7} \, \mathrm{cm}^3 \, \mathrm{s}^{-1}/m_i$ and $\xi_{\mathrm{CR}} \approx 10^{-17} \, \mathrm{s}^{-1} \, (m_i/m_n)$ in this study (see, e.g., Shu 1992; Tielens 2005), where $m_n = 2.3\times$ and $m_i = 30\times$ the hydrogen mass are considered. Indeed, $\chi_{i0} = 10$ falls in the typical range of χ_{i0} observed in star-forming regions ($\sim1-20$; see, e.g., McKee et al. 2010). The fiducial model is selected such that it can be reproduced easily by comparison with the results of CO12.

Without loss of generality, we adopt a constant wavenumber (k) of $1/0.015 \, \mathrm{pc}^{-1}$ to keep the fiducial model as simple as possible. Figure 1 displays the r_n/r_B ratio of the background state (left panel) and the validity of the WKBJ approximation (right panel). The C-shock transition begins from $x = 0$ pc and ends at approximately $x = 0.4$ pc. We obtained the same U-shape for the r_n/r_B ratio as that obtained by CO12 in their Figure 3. The U-shaped profile is a notable feature of the C-shock model, as demonstrated by CO12. The ratio $r_n/r_B = 1$ in the pre- ($x < 0$ pc) and postshock ($x > 0.4$ pc) regions where no background gradients are present. Throughout the C-shock, $1/(kL_B)$ and $1/(kL_p)$ are considerably smaller than 1; thus, the WKBJ approximation is justified. The marginally high value of $1/(kL_B)$ and $1/(kL_p)$ around $x = 0$ pc and $x = 0.4$ pc, respectively, is caused by the initial compression of the ions and thus the magnetic fields, followed by a delayed compression of the neutrals by means of the ion–neutral drag as the gas flows downstream across the steady C-shock.

2.3. Dispersion Relations

Before solving the eigenvalue problem in Equation (14), we analyze Equation (14) in terms of a couple of simplified dispersion relations, which will provide the basic and clear
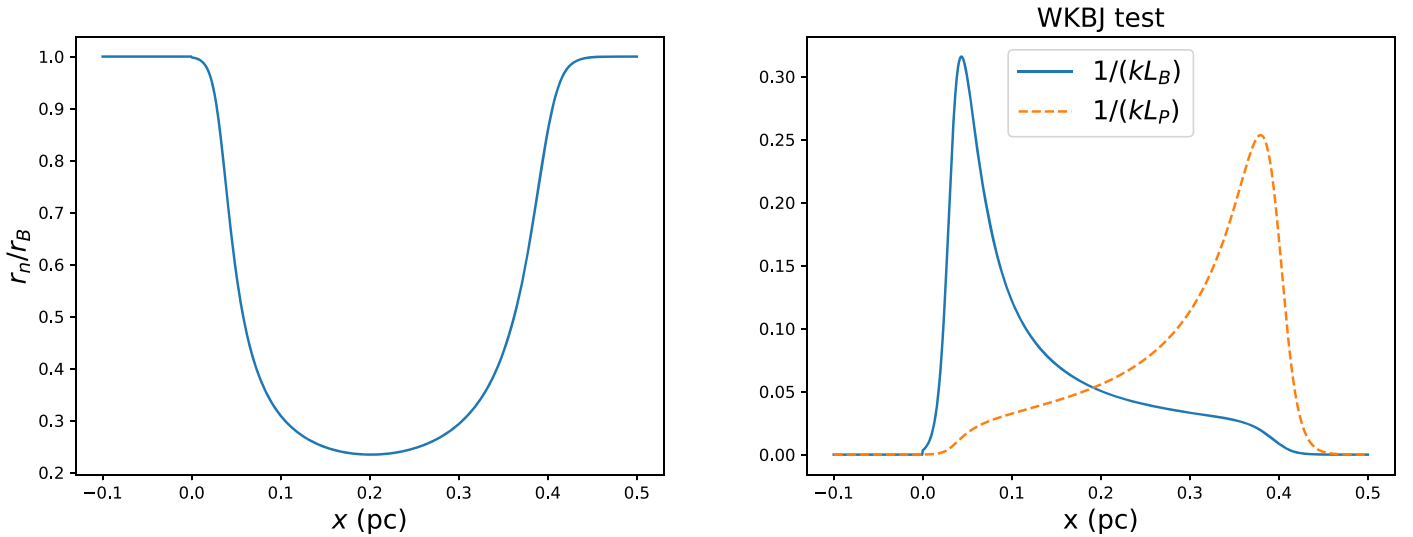
Figure 1. The r_n/r_B ratio of the background state throughout the C-shock (left panel) and a test for the WKBJ approximation when $k = 1/0.015$ pc^{-1} (right panel). $L_p \equiv |d \ln p/dx|^{-1}$ and $L_B \equiv |d \ln B/dx|^{-1}$ are the scale heights for the gas pressure and magnetic field of the background states, respectively.

Table 1
Summary of the Main Symbols Adopted in the Linear Analysis

Symbol and definition	Meaning
$\Gamma \equiv i\omega + ikV_n$	rate of a mode in the comoving frame of the neutrals
Γ_{GLV}	rate of the unstable/decaying mode derived by GLV
$\Gamma_{re} \equiv 2\beta\rho_i$	recombination rate
$\Gamma_{grav} \equiv \sqrt{G\rho_n}$	rate of the gravitational instability
$\Gamma_{th} \equiv kc_s$	sound-crossing rate over one wavelength
$\Gamma_{kV_d} \equiv k|V_d|$	ion–neutral drift rate across a distance of wavelength
$\Gamma_{alf,i} \equiv kV_{A,i}$	speed of the Alfvén wave in the ions crossing one wavelength
$\Gamma_{alf,n} \equiv kV_{A,n}$	speed of the Alfvén wave in the neutrals crossing one wavelength
$\Gamma_{ambi} \equiv k^2 D_{ambi}$	ambipolar diffusion rate
$\gamma_n \equiv \gamma\rho_n$	ion collision rate with the neutrals
$\gamma_i \equiv \gamma\rho_i$	neutral collision rate with the ions
Γ_{grow}	growth rate of an unstable mode
$\omega_{wave,n}$	wave frequency of an unstable mode in the comoving frame of the neutrals
$\omega_{wave} \equiv \text{Re}[\omega]$	wave frequency of a mode
$D_{ambi} \equiv V_{A,n}^2/\gamma\rho_i$	ambipolar diffusion coefficient
$\gamma \approx 3.5 \times 10^{13}$ cm^3 s^{-1} g^{-1}	drag force coefficient (Draine et al. 1983)

physics to better understand the exact solutions obtained using the eigenvalue approach. Table 1 summarizes the meanings of the main symbols that we use in the linear analysis.

The analysis begins with a brief review of the drag instability. GLV indicated that when the drift velocity V_d is sufficiently high, a type of overstability, called the drag instability, can occur. Specifically, for the definite occurrence of the instability, the rate of the mode $\Gamma \equiv i\omega + ikV_n$ observed in the comoving frame of the neutrals is considerably lower than both the recombination rate $\Gamma_{re} \equiv 2\beta\rho_i$ and the ion–neutral drift rate across a distance of wavelength (i.e., $\Gamma_{kV_d} \equiv k|V_d|$), whereas it is considerably higher than the neutral collision rate with the ions (i.e., $\gamma_i \equiv \gamma\rho_i$), the sound-crossing

rate over one wavelength (i.e., $\Gamma_{th} \equiv kc_s$), and the rate of the gravitational instability (i.e., $\Gamma_{grav} \equiv \sqrt{G\rho_n}$). Although self-gravity is not included in our equations, Γ_{grav} is still estimated to evaluate its significance. When the aforementioned conditions are satisfied, the linearized equation (Equation (14)) is substantially reduced to (see GLV)

$$\Gamma\frac{\delta\rho_n}{\rho_n} = ik\delta v_n, \tag{16}$$

$$\Gamma\delta v_n \approx \gamma\rho_i V_d \frac{\delta\rho_i}{\rho_i}, \tag{17}$$

$$2\beta\rho_i \frac{\delta\rho_i}{\rho_i} \approx \xi_{CR} \frac{\rho_n}{\rho_i}\frac{\delta\rho_n}{\rho_n}. \tag{18}$$

Along with the background states, the above equations leads to the dispersion relation,

$$\Gamma_{GLV} \approx \pm\frac{(1+i)}{2}\sqrt{\Gamma_{kV_d}\gamma_i} = \pm\frac{(1+i)}{2}\sqrt{\frac{k}{L_B}}V_{A,n}. \tag{19}$$

In the above dispersion relation, the positive and negative parts correspond to the growing and decaying waves, respectively. The subscript GLV is added to Γ to indicate the growth/damping rate ($\text{Re}[\Gamma]$) and wave frequency ($\text{Im}[\Gamma]$) of the unstable/decaying mode derived by GLV, which is compared to the eigenvalue of the growing mode in Section 2.4. The growth/damping rate is lower than the speed of the Alfvén wave in the neutrals crossing one wavelength $\Gamma_{alf,n} \equiv kV_{A,n}$, which indicates that the unstable/decaying mode is slower than the magneto-acoustic mode of the bulk fluid. It is also evident that the above dispersion relation appears very different from that for the magneto-acoustic mode, and therefore the density perturbation is not caused by magneto-acoustic oscillations.[3] The reason why the 1D overdensity/underdensity occurs in the bulk of the fluid (i.e., the neutrals) is that the neutrals experience high drag due to the density clump of the ions

---

[3] In this regard, the unstable mode is "incompressible."
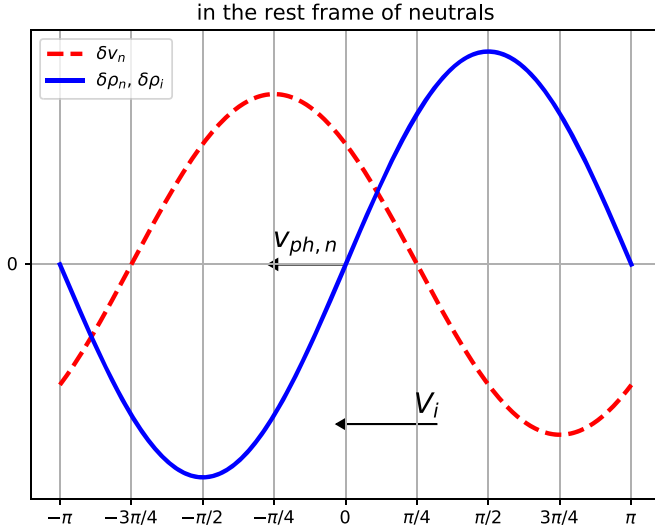
Figure 2. Phase diagram of the drag instability in the rest frame of the neutrals. The profiles of δv_n and $\delta \rho_n$ as a function of x are displayed, and the directions of V_i and $v_{ph,n}$ are indicated. The amplitudes of the perturbations are shown on arbitrary scales.

(Equation (17)), which is also the density clump of the neutrals due to the rapid ionization equilibrium (Equation (18)).

By substituting the positive part of Equation (19) (for an unstable wave) into Equation (16), we have the relation $\delta v_n \propto \delta \rho_n \exp(i3\pi/4)$ and obtain the phase velocity in the comoving frame of the neutrals given by $v_{ph,n} = -\mathrm{Im}[|\Gamma_{GLV}|]/k < 0$. These imply that v_n leads $\delta \rho_n$ by a phase of $3\pi/4$, and the unstable wave travels upstream in the rest frame of the neutrals. As explained in GLV, this specific phase difference between δv_n and $\delta \rho_n$ in the rest frame of neutrals is the physical origin of the drag instability. Figure 2 illustrates how the instability occurs. The ion and neutral density perturbations $\delta \rho_i$ and $\delta \rho_n$ are in phase due to the ionization equilibrium. In the rest frame of the neutrals, the wave and V_i propagate upstream (to the left), and δv_n leads $\delta \rho_n$ by a phase difference $3\pi/4$. Consequently, the peak of the density perturbation $\delta \rho_n$ at $x = \pi/2$ continues to increase due to the converging velocity field (i.e., $d\delta v_n/dx < 0$), while the trough of the density perturbation at $x = -\pi/2$ continues to decrease due to the diverging velocity field (i.e., $d\delta v_n/dx > 0$), thereby leading to further growth of the perturbations. We refer to the study of GLV for more detailed descriptions.[4] Note that the unstable wave in fact propagates downstream in the shock frame at the phase velocity given by $v_{ph,n} + V_n$: the fast streaming motion of the background flow brings the growing wave downstream through the shock.

We now examine the dispersion relations outside a C-shock where $V_i = V_n$. Thus, $V_d = 0$ and $\Gamma_i \equiv i\omega + ikV_i = \Gamma$ in both the pre- and postshock regions. Hence, the dispersion relation derived from Equation (14) reads (e.g., GLV)

$$\Gamma_{th}^4 \Gamma + \Gamma \Gamma_{re}[\Gamma_{alf,i}^2(\Gamma + \gamma_i) + \Gamma^2 \gamma_n]$$
$$+ \Gamma_{th}^2\left[\Gamma_{alf,i}^2 \Gamma_{re} + \Gamma(2\Gamma + \gamma_i)\frac{\Gamma_{re}}{2} + \Gamma\Gamma_{re}\gamma_n\right] = 0, \quad (20)$$

where $\Gamma_{alf,i} \equiv kV_{A,i}$ and $\gamma_n \equiv \gamma\rho_n$. The rate Γ_{th} usually has a low value. It may be even lower than γ_i in the above dispersion relation, which sometimes occurs in the postshock region where the neutral density is compressed and the ion density is subsequently enhanced by ionization. Ignoring the thermal terms associated with Γ_{th} at this moment, Equation (20) can be reduced as

$$(\Gamma + \Gamma_{re})[(\Gamma_{alf,i}^2 + \Gamma^2)(\Gamma + \gamma_i) + \gamma_n\Gamma^2] = 0. \quad (21)$$

The first term of the above equation represents a decaying mode with a damping rate of $-\Gamma_{re}$. In the second term of the above equation, we have recovered the well-known dispersion relation for 1D linear Alfvén waves in a weakly ionized plasma (Kulsrud & Pearce 1969).[5] Two branches of this mode can exist depending on the strength of the coupling between ions and neutrals (i.e., the strong and weak-coupling branches). In the strong-coupling branch, $\Gamma_{alf,i} \ll \gamma_n$; thus, the dispersion relation can be further reduced as follows (e.g., Kulsrud & Pearce 1969; McKee et al. 2010):

$$\omega + kV_n = \pm\left(\Gamma_{alf,i}^2 \frac{\rho_i}{\rho_n} - \frac{\Gamma_{alf,i}^4}{4\gamma_n^2}\right)^{1/2} + i\frac{\Gamma_{alf,i}^2}{2\gamma_n}$$
$$\approx i\left[\frac{\Gamma_{ambi}}{2} \pm \left(\frac{\Gamma_{ambi}}{2} - \gamma_i\right)\right], \quad (22)$$

where Γ_{ambi} is the ambipolar diffusion rate equal to $k^2 D_{ambi}$, with the ambipolar diffusion coefficient $D_{ambi} \equiv V_{A,n}^2/\gamma\rho_i$. We have assumed that $\Gamma_{ambi} \gg \Gamma_{alf,n}$ to expand the expression of the square root to further simplify the final result on the right-hand side of Equation (22). On the other hand, the dispersion relation is obtained for the weak-coupling regime (Kulsrud & Pearce 1969; McKee et al. 2010),

$$\omega + kV_n = \pm\left(\Gamma_{alf,i}^2 - \frac{\gamma_n^2}{4}\right)^{1/2} + i\frac{\gamma_n}{2}$$
$$\approx i\left[\frac{\gamma_n}{2} \pm \left(\frac{\gamma_n}{2} - \Gamma_{ambi}\right)\right], \quad (23)$$

where we have assumed that $\gamma_n^2 \gg \Gamma_{ambi}^2$, which is equivalent to $\gamma_n \gg \Gamma_{alf,i}$, to expand the expression of the square root to derive the right-hand side of Equation (23). Thus, Equations (22) and (23) indicate that no waves but decaying modes exist in the frame comoving with the flow. The damping rates in the strong-coupling branch are $\sim\Gamma_{ambi}$ and γ_i, and the damping rates in the weak-coupling branch are $\sim\gamma_n$ and Γ_{ambi}.

Finally, there exist slow decaying modes associated with the weak thermal effect that we have ignored so far. When we consider that $\Gamma \ll \Gamma_{alf,i}$, γ_i and because $\Gamma_{th} \ll \Gamma_{ambi}$, Equation (20) can be reduced to $\Gamma_{th}^2 + \Gamma^2 + \Gamma\gamma_i \approx 0$, which has two solutions: $\Gamma \approx (-\gamma_i \pm \sqrt{\gamma_i - 4\Gamma_{th}^2})/2$. If $\gamma_i^2 \gg 4\Gamma_{th}^2$, the reduced dispersion relation yields the following two decaying modes with no waves in the comoving frame of the

---

[4] In the study of GLV, $V_d > 0$ and thus δv_n leads $\delta \rho_n$ by a phase of $\pi/4$ instead of $3\pi/4$ in the comoving frame of the neutrals. Nevertheless, the image for the drag instability is the same.

[5] Kulsrud & Pearce (1969) used the perturbations $\propto\exp(ikx - i\omega t)$, whereas we use the perturbations $\propto\exp(ikx + i\omega t)$ and consider a background flow that produces the Doppler-shifted frequency kV_n.
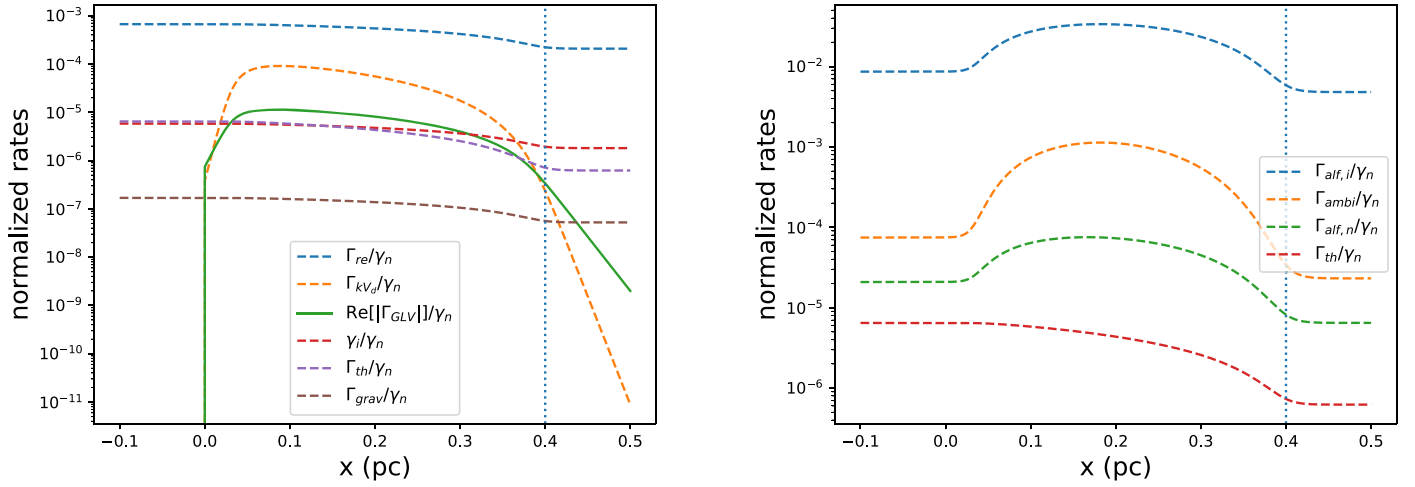
Figure 3. Comparison of various rates relevant to the assumptions for the derivation of dispersion relations, normalized by γ_n throughout the C-shock in our fiducial model (left panel). Additional normalized rates relevant to the postshock regions are also plotted and compared (right panel). The domain to the right of the vertical dotted line represents the postshock region.

flow:

$$\omega + kV_n \approx i\frac{\Gamma_{th}^2}{\gamma_i}, \, i\gamma_i. \tag{24}$$

However, if $\gamma_i^2 \ll 4\Gamma_{th}^2$, the following two decaying wave modes exist in the comoving frame of the flow:

$$\omega + kV_n \approx i\frac{\gamma_i}{2} \pm \Gamma_{th}. \tag{25}$$

In summary, the dispersion relation in the postshock region (Equation (20)) indicates the presence of five decaying modes with damping rates of γ_n, $2\beta\rho_i$, Γ_{ambi}, γ_i, and Γ_{th}^2/γ_i when $\Gamma_{th} < \gamma_i$ or γ_n, $2\beta\rho_i$, Γ_{ambi}, $\gamma_i/2$, and $\gamma_i/2$ (the same as for the two slowest modes) when $\Gamma_{th} > \gamma_i$.

Figure 3 illustrates the suitability of the assumptions made in our fiducial C-shock model, where k is set to $1/0.015 \, \text{pc}^{-1}$; the assumptions were made to derive the dispersion relations inside and outside the C-shock. The left panel of Figure 3 indicates that the ion–neutral drift rate across one wavelength, Γ_{kV_d}, becomes high within the C-shock (i.e., between $x = 0$ and $x \approx 0.4 \, \text{pc}$) because of the high drift velocity V_d that is caused by the shock compression. Consequently, Γ_{kV_d} is higher than γ_i but still lower than Γ_{re} and γ_n inside the C-shock. The drag instability thus occurs inside the shock according to the dispersion relation presented in Equation (19), with the growth rate $Re[\Gamma_{GLV}]$ being higher than γ_i and Γ_{th}. Although we plot Γ_{GLV} beyond $x \approx 0.4 \, \text{pc}$ in the postshock region, the instability is expected to disappear because Γ_{kV_d} decreases quickly outside the C-shock. We also plot the rate of gravitational instability Γ_{grav}, which is considerably lower than the other rates and can be reasonably neglected in the linear analysis.

The right panel of Figure 3 indicates that $\gamma_n \gg \Gamma_{alf,i} \gg \Gamma_{ambi} \gg \Gamma_{alf,n}$, which ensures the presence of the decaying modes described by the dispersion relations with $V_d = 0$, i.e., Equations (22) and (23), in the postshock region. We also see from the figure that Γ_{th} is the lowest rate of the rates of interest. It can be ignored except when $\Gamma \lesssim \Gamma_{th}$, which results in the presence of two modes of the lowest decaying rate associated with γ_i and Γ_{th} in the postshock region, as described by Equations (24) and (25). In the fiducial model, the left panel of Figure 3 shows that $\gamma_i > \Gamma_{th}$ in the postshock region. Hence, the decaying mode is

expected to follow the dispersion relation described by Equation (24) more closely (see the next subsection).

### 2.4. Exact Solutions Obtained from the Eigenvalue Problem

After identifying the modes and determining their underlying physics through the simple dispersion relations, we study the exact solutions of the entire set of linearized equations in Equation (14). Figure 4 shows the properties of the eigenvalues, which describe the behaviors of the growth/damping rates (left panel) and the wave frequencies for the modes of interest (right panel). The left panel of Figure 4 overplots the five eigenvalues $Im[\omega]$ at four different locations (colored dots), both inside ($x = 0.1$, 0.2, 0.3 pc) and outside ($x = 0.5$ pc) the C-shock, with relevant rates in the system. Of the five eigenmodes, only one unstable wave mode exists inside the C-shock (red dots). In contrast, there are only decaying wave modes (blue dots) in the postshock region (the $x = 0.5$ pc location).

To understand the properties of these eigenvalues, the left panel of Figure 4 also shows the rates relevant to the different decaying modes according to the dispersion relations in the previous subsection. We see that the first three largest $Im[\omega]$ are almost the same as γ_n, Γ_{ambi}, and Γ_{re} and therefore correspond to the the damping processes due to ion–neutral collisions, ambipolar diffusion, and recombination, respectively. Although the result is expected from the dispersion relations for the postshock region, the left panel of Figure 4 suggests that the aforementioned three damping modes also exist inside the shock. In addition, Figure 4 also illustrates that the two smallest $Im[\omega]$ at $x = 0.1$, 0.2, and 0.3 pc are consistent with $Re[\Gamma_{GLV}]$ for the pair of growing and decaying wave modes.

Furthermore, the left panel of Figure 4 shows that the last two smallest $Im[\omega]$ are close to γ_i and Γ_{th}^2/γ_i at $x = 0.5$ pc; thus these eigenvalues are consistent with the dispersion relations for $\gamma_i > \Gamma_{th}$ in the postshock region, as expected from the previous subsection. When k is increased such that $\gamma_i \approx \Gamma_{th}$ or even $\gamma_i \ll \Gamma_{th}$, the decaying rate of the modes with the last two smallest $Im[\omega]$ becomes close to $\gamma_i/2$ in the postshock region (not shown), in accordance with the dispersion relation described by Equation (25) or the more general form
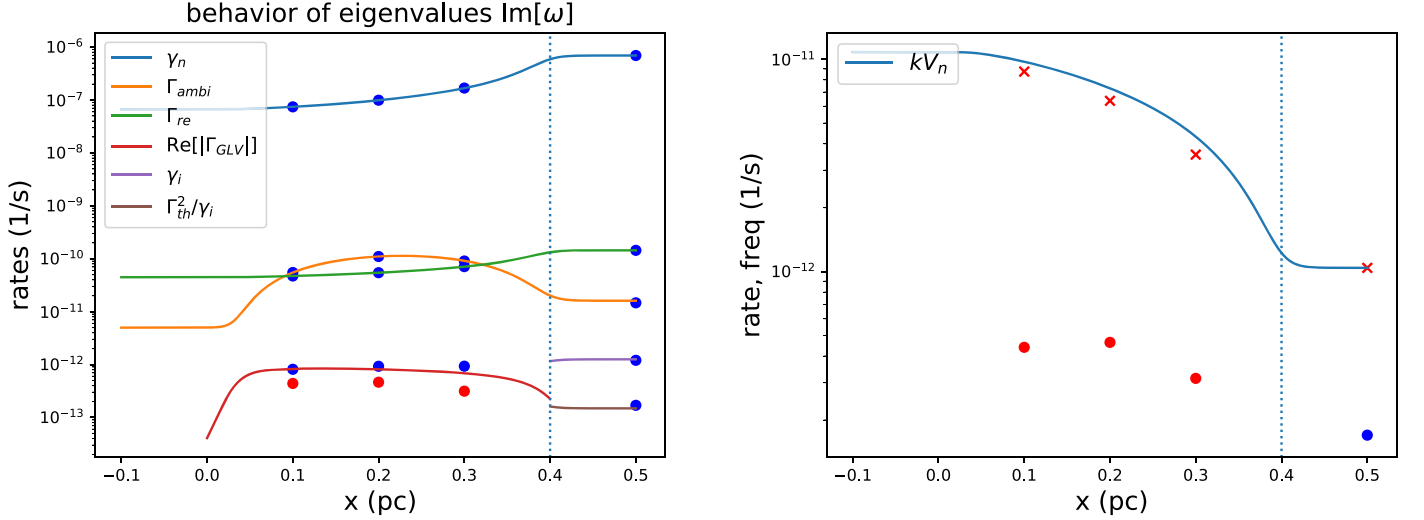
Figure 4. Properties of the eigenvalues in the shock and postshock regions in the fiducial model. The left panel shows 5 eigenvalues Im[||ω||] at $x = 0.1, 0.2, 0.3,$ and 0.5 pc in terms of blue (Im[ω] > 0 indicative of a damping rate) and red (Im[ω] < 0 indicative of a growth rate) dots. The curves for various rates relevant to the eigenvalue ω are overplotted for comparison. The right panel shows the wave frequencies Re[$-\omega$] (red crosses) associated with the modes with the smallest Im[||ω||] (colored dots), i.e., the unstable modes inside the shock and the mode with the slowest damping rate in the postshock region. The curve for kV_n is also plotted for comparison. The domain to the right of the vertical dotted line ($x \approx 0.4$ pc) in the two panels is the postshock region.
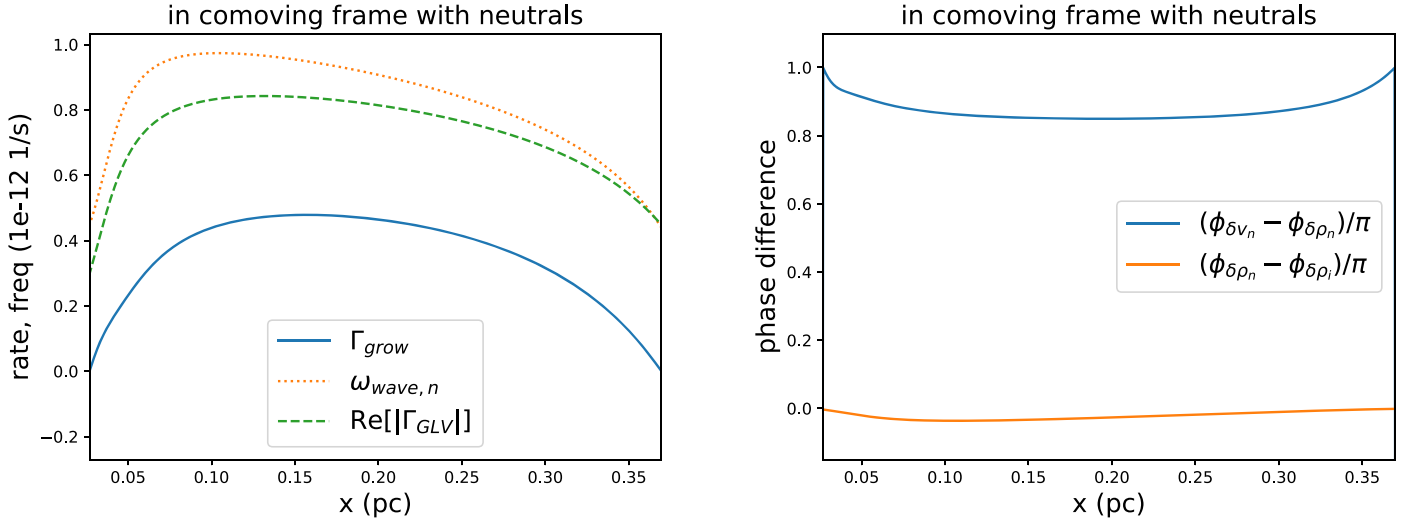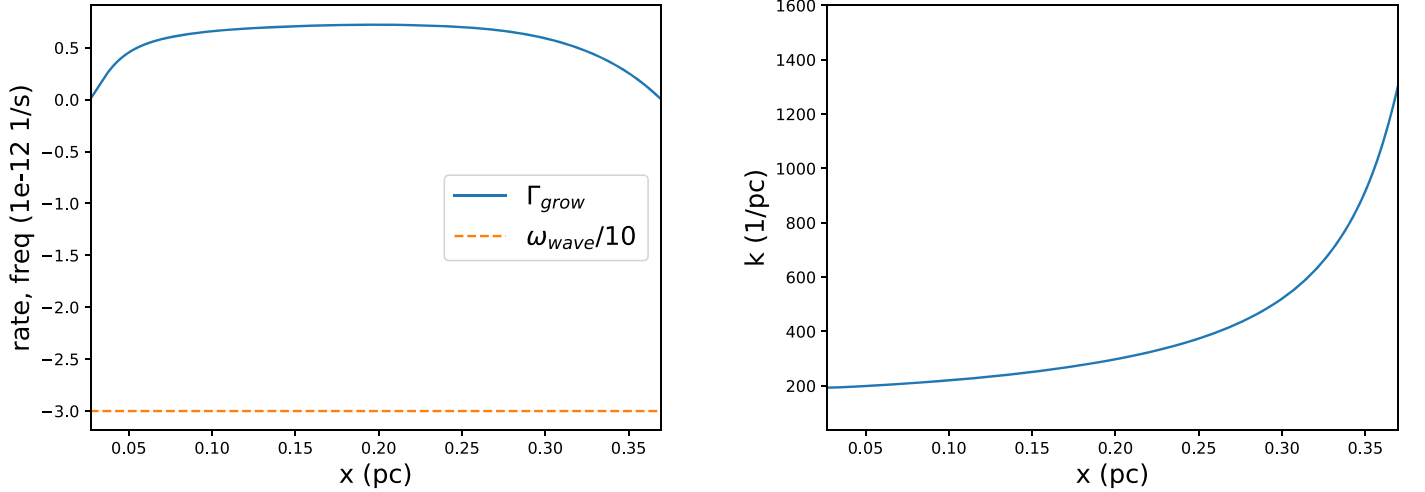

Figure 5. The growth rate Γ_{grow} and wave frequency $\omega_{\text{wave},n}$ of the unstable mode seen by the neutrals are plotted in comparison with the growth rate Re[Γ_{GLV}] estimated by GLV (left panel). The phase difference between the velocity and density perturbations of the neutrals ($\phi_{\delta v_n} - \phi_{\delta \rho_n}$) and the phase difference between the density perturbation of the neutrals and the ions ($\phi_{\delta \rho_n} - \phi_{\delta \rho_i}$) are also displayed within the C-shock (right panel).

$\Gamma = -\gamma_i \pm \sqrt{\gamma_i^2 - 4\Gamma_{\text{th}}^2}/2$ shown in Section 2.3. Combined with the fact that these two modes represent the pair of the growing and decaying wave modes within the C-shock (see Equation (19)), this suggests that these two decaying modes in the postshock region replace the overstable mode and its counterpart of decaying mode inside the shock. We trace the evolution of the eigenvalue and eigenmode from the in-shock to the postshock region around $x \approx 0.4$ pc. We find that when the overstable mode propagates to the postshock region, it gradually transforms into a decaying mode with the damping rate of $\approx \Gamma_{\text{th}}^2 / \gamma_i$ in our fiducial case.

Figure 5 illustrates the physical properties of the unstable mode as a function of x in the comoving frame of the neutrals. The left panel of Figure 5 displays the growth rate Γ_{grow} ($= -\text{Im}[\omega] > 0$) and wave frequency $\omega_{\text{wave},n}$ ($= \text{Re}[\omega] + kV_n$) of the unstable mode in the comoving frame of the neutrals.

The growth rate Re[||Γ_{GLV}||] is also plotted in this panel for comparison. According to the simplified dispersion relation in Equation (19), Re[||Γ_{GLV}||] = $\omega_{\text{wave},n}$ = Γ_{grow}. These parameters are not completely identical for the exact solutions shown in left panel of Figure 5, however; $\omega_{\text{wave},n}$ and Re[||Γ_{GLV}||] are marginally larger than Γ_{grow} due to the presence of less dominant terms that are not significantly smaller than Re [||Γ_{GLV}||], such as γ_i and Γ_{th} (left panel of Figure 3). Owing to the same reason, the phase difference between δv_n and $\delta \rho_n$ of the unstable model is not exactly $(3/4)\pi$, as expected from the dispersion relation, but approaches this toward $\approx 0.85\pi$ from the shock boundaries to the middle of the shock width, as depicted in the right panel of Figure 5. The same panel also shows that $\delta \rho_n$ and $\delta \rho_i$ are almost in phase due to the ionization-recombination equilibrium. When we remove the ionization and recombination terms in the linearized equations, the unstable mode almost disappears in the eigenvalue

Figure 6. Profiles of the growth rate Γ_{grow} (left panel) and the corresponding wavenumber k (right panel) of the unstable mode with the wave frequency (ω_{wave}) of $-3 \times 10^{-11} \, \text{s}^{-1}$, which is indicated by the dashed orange line in the left panel.

problem. Consequently, the overall results are consistent with the results expected from the simple dispersion relation for the drag instability. The physical picture is that in the comoving frame of the neutrals, the ions drift toward the shock front at $x = 0$ pc ($V_d < 0$), and the wave travels toward the shock front as well ($\omega_{\text{wave},n} > 0$) with a phase of δv_n, which leads $\delta \rho_n$ by approximately $(3/4)\pi$.

Because the overstable mode propagates inside the shock and subsequently decays in the postshock region, a problem arises regarding whether sufficient time is available for the unstable wave to grow. The right panel of Figure 4 shows the smallest $\text{Im}[|\omega|]$ (dots) and its corresponding wave frequency $\text{Re}[-\omega]$ (crosses) inside the C-shock at $x = 0.1$, 0.2, and 0.3 pc and in the postshock region at $x = 0.5$ pc for our fiducial model with $k = 1/(0.015 \, \text{pc})$. The ratio $\text{Re}[-\omega]/\text{Im}[|\omega|]$ is approximately 10–20, which indicates that unstable waves travel downstream approximately 1020 times faster than their growth rate. This high rate of wave propagation in the shock frame is caused by the advection of waves by the fast downstream motion with a speed of V_n, which dominates $v_{ph,n}$ of the unstable mode. The aforementioned statement is verified by the result $\text{Re}[-\omega] \approx k V_n$, as presented in the right panel of Figure 4. In particular, $\text{Re}[-\omega]$ is exactly equal to kV_n in the postshock region, which agrees with the dispersion relations. In the following section, we investigate whether the shock width is sufficient or if any favorable preshock conditions exist for the fast-traveling wave to grow significantly.

3. Total Growth of an Unstable Wave Over the Shock Width

3.1. The Maximum-growth Mode

In the preceding WKBJ analysis, we simply kept k constant in the fiducial case to study the basic properties of a local unstable/decaying mode. To examine whether an unstable wave mode can grow appreciably over the shock width, we consider a mode of a given wave frequency of $\omega_{\text{wave}} = \text{Re}[\omega]$ in the shock frame (e.g., $\sim -1 \times 10^{-11} \, \text{s}^{-1}$ according to the right panel of Figure 4). Equation (14) is solved for both the growth rate Γ_{grow} ($\equiv \text{Im}[\omega]$ when $\text{Im}[\omega] < 0$ or zero otherwise) and the wavenumber k, corresponding to a given ω_{wave}

everywhere in the shock. The perturbation amplitude $|U|$ is arbitrary in a linear analysis for normal modes. For our purpose of evaluating the global growth, we can gain a general sense of the total growth of the unstable model U by setting its norm equal to 1 everywhere in the shock. The local growth of the unstable wave mode is $\exp[\Gamma_{\text{grow}}(dx/v_{\text{ph}})]$, where v_{ph} is the phase velocity of the wave in the shock frame and is equal to $-\omega_{\text{wave}}/k$. Consequently, the total growth of the mode can be computed by integrating the local growth over the entire shock width (i.e., $\exp(\int_{\text{shock width}} \Gamma_{\text{grow}} dx/v_{\text{ph}})$). We vary the wave frequency ω_{wave} and repeat the above procedure to seek the particular mode with the maximum total growth (MTG). MTG=1 when no growth occurs (i.e., $\Gamma_{\text{grow}} = 0$ everywhere).

In our fiducial model for the steady C-shock, the mode $\omega_{\text{wave}} \approx -3 \times 10^{-11} \, \text{s}^{-1}$ is responsible for the MTG. The mode properties as a function of x are shown in Figure 6. The figure indicates that the growth rate Γ_{grow} increases from the shock front around $x \gtrsim 0.027$ pc, declines after the midpoint of the shock width, and then drops to zero at the end of the shock width at approximately $x = 0.37$ pc. The parameter Γ_{grow} is more than 10 times smaller than ω_{wave}. Nevertheless, the wavenumber k increases downstream across the shock width due to the gradient of the background states. The result can be explained by the relation $\text{Re}[-\omega] \approx k V_n$, as discussed in the preceding section. Because the wave frequency ω_{wave} ($=\text{Re}[\omega] \approx - k V_n$) is approximately constant for a given wave mode, V_n decreases and hence k increases with x as the neutrals are compressed and thus decelerated downstream inside the shock.

The left panel of Figure 7 indicates that $1/(kL_B)$ and $1/(kL_p)$ of the unstable mode are considerably smaller than 1, which justifies the WKBJ approximation for the calculations. The right panel of Figure 7 displays the profile of the exponential exponent of the local growth ($\Gamma_{\text{grow}} dx/v_{\text{ph}}$) across the shock. The profile indicates that the unstable mode gains more growth in the rear of the shock transition because the mode has a larger k farther downstream within the shock and hence propagates more slowly to allow for more growth. This maximum-growth mode caused by the drag instability results in an MTG value of approximately 9.9 within the steady C-shock, which implies that an initial perturbation of finite magnitude (i.e.,
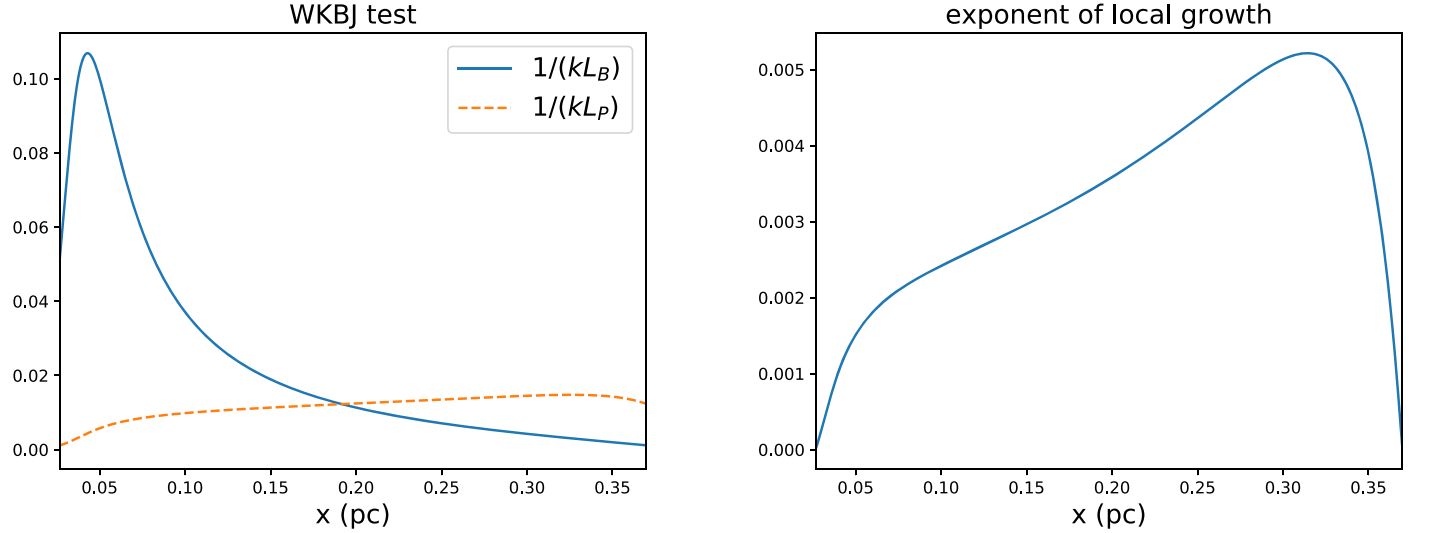
Figure 7. WKBJ test for the unstable mode with $\omega_{\rm wave} = -3 \times 10^{-11}\,{\rm s}^{-1}$ (left panel) and the profile of the exponent of the local growth (right panel) in the fiducial model.

Table 2
MTG and Corresponding Mode Frequency $\omega_{\rm wave}$ of the Drag Instability in the Steady C-shock Models of CO12

Model	n_0 (cm^{-3})	v_0 (km s^{-1})	B_0 (μG)	χ_{i0}	$L_{\rm shock}$ (pc)	$\omega_{\rm wave}$ (s^{-1})	MTG
N01	100	5	10	5	3.15	$-2{\rm e}-11$	10.9
N03	300	5	10	5	1.38	$-3{\rm e}-11$	19.1
N05	500	5	10	5	0.94	$-3{\rm e}-11$	22.0
N08	800	5	10	5	0.66	$-4{\rm e}-11$	23.8
N10	1000	5	10	5	0.56	$-4{\rm e}-11$	24.7
V04	200	4	10	5	1.68	$-3{\rm e}-11$	6.4
V06	200	6	10	5	2.05	$-2{\rm e}-11$	36.0
V08	200	8	10	5	2.37	$-2{\rm e}-11$	121.2
V10	200	10	10	5	2.65	$-4{\rm e}-11$	327.3
V12	200	12	10	5	2.90	$-3{\rm e}-11$	816.2
B02	200	5	2	5	0.84	$-2{\rm e}-11$	27.7
B04	200	5	4	5	1.18	$-2{\rm e}-11$	25.3
B06	200	5	6	5	1.45	$-2{\rm e}-11$	22.5
B08	200	5	8	5	1.68	$-2{\rm e}-11$	19.5
B10	200	5	10	5	1.87	$-2{\rm e}-11$	16.6
B12	200	5	12	5	2.05	$-2{\rm e}-11$	13.7
B14	200	5	14	5	2.22	$-2{\rm e}-11$	11.2
X01	200	5	10	1	9.37	$-2{\rm e}-11$	23.5
X06	200	5	10	6	1.56	$-2{\rm e}-11$	14.7
X10	200	5	10	10	0.94	$-2{\rm e}-11$	8.9
X15	200	5	10	15	0.62	$-2{\rm e}-11$	5.1
X20	200	5	10	20	0.47	$-1{\rm e}-11$	3.6
Fig4CO12	200	1	2	10	0.18	$-8{\rm e}-12$	1.05
Fig5CO12	500	1	4	10	0.13	N/A	1

Note. The final two rows correspond to the two additional models used for Figures 4 and 5 in CO12, respectively. The parameter $L_{\rm shock}$ is the shock width estimated using Equation (42) in CO12.

$\delta\rho_n/\rho_n \sim 1/10$) is required for a substantial growth of the mode to the nonlinear regime.

3.2. A Parameter Study

In addition to the fiducial case, we also calculate the MTG for the C-shock models listed in Table 1 of CO12, which represent various conditions for C-shocks to form in star-forming clouds. The results of the parameter study are presented in Table 2. In accordance with CO12, the letters N, V, B, and X of the model names denote the variations in the n_0, v_0, B_0, and χ_{i0} values of the models, respectively. In this study,

the variation in χ_{i0} is simply calculated by changing the recombination rate β while maintaining the ionization rate $\xi_{\rm CR}$ constant. Table 2 is almost identical to Table 1 of CO12, except for the last two columns, which present the MTG and the corresponding $\omega_{\rm wave}$ of the unstable mode in each model.

Table 2 indicates that for the unstable modes with the MTG, $\omega_{\rm wave}$ has a low model dependence and has the value of approximately 1–$4 \times 10^{-11}\,{\rm s}^{-1}$. In Table 2, the MTG exhibits an increasing trend with the increasing n_0 and v_0 but decreasing B_0 and χ_{i0}. A wider shock width $L_{\rm shock}$ does not necessarily result in a larger MTG. The MTG changes by approximately 10-20 times due to the variations in n_0, B_0, and χ_{i0} in the

parameter study, resulting in a modest mode growth as in the fiducial model. By comparison, the MTG is more sensitive to the change in v_0. In the parameter study, the stronger shocks characterized by higher shock speeds ($v_0 = 8$–12 km s^{-1}) with wider shock widths ($L_{shock} \gtrsim 2$ pc), as presented in Models V08, V10, and V12, can boost the MTG to a value of several hundred.

In addition to considering the original models in Table 1 of CO12, we ran two additional models, which are denoted as "Fig4CO12" and "Fig5CO12" in the last two rows of Table 2. These two models correspond to the scenarios shown in Figures 4 and 5 of CO12 for their 1D MHD simulations, which represent the interesting cases of weak C-shocks with $v_0 = 1$ km s^{-1}. The MTG values of these two cases are almost 1, meaning little to no growth of the initial perturbation for weak C-shocks.

The overall trend of the change in the MTG with the preshock parameters n_0, v_0, B_0, and χ_{i0} may be qualitatively but not quantitatively understood as follows: The exponent of the MTG (i.e., $\int_{\text{shock width}} \Gamma_{\text{grow}} dx / v_{\text{ph}}$) can be approximated to $t_{ad} \Gamma_{\text{grow}}$, where t_{ad} is the ambipolar drift timescale across the shock width, which is equal to L_{shock}/V_d. Inside the shock, the ions are compressed prior to the neutrals. Thus, we consider $r_n \sim 1$ and $r_B \sim r_f$, where r_f is the final compression ratio, which is proportional to $v_0/V_{A,n,0}$ (CO12). Using the dispersion relation $\Gamma_{\text{grow}} \sim \sqrt{k/L_B} V_{A,n} \approx \sqrt{\omega_{\text{wave}}/(L_B V_n)} V_{A,n}$ as well as $L_B \sim L_{shock}$, $V_d \sim V_n \sim v_0/r_f$, and $V_{A,n} \propto B n_n^{-1/2} \propto (r_B B_0)(r_n n_0)^{-1/2}$, we obtain the following relations: $V_{A,n} \sim v_0$ and $V_d \sim V_{A,n,0}$. Because $L_{shock} \propto n_0^{-3/8} v_0^{1/4} B_0^{1/4} \chi_{i0}^{-1/2}$ (CO12), it follows that $t_{ad} \Gamma_{\text{grow}} \propto L_{shock}^{1/2} V_d^{-3/2} v_0 \propto n_0^{3/8} v_0^{5/4} B_0^{-5/4} \chi_{i0}^{-1/2}$. The scaling result for the exponent qualitatively gives the trend that MTG increases with n_0 and v_0, but decreases with B_0 and χ_{i0}. In terms of a rough physical picture, the ion–neutral drift velocity, which is comparable to the neutral Alfvén velocity in the preshock region, is enhanced by strong magnetic fields or a low neutral density, leading to a short ambipolar drift time t_{ad} for the unstable wave to grow. Hence, a positive correlation exists between the MTG and the neutral density n_0, whereas a negative correlation exists between the MTG and the magnetic fields B_0. In addition, the neutral Alfvén speed in the shock is enhanced in a strong shock to result in a high growth rate; that is, a positive correlation between the MTG and the shock speed v_0. Finally, χ_{i0} changes the MTG by varying the shock width. A large χ_{i0} leads to a wide shock width, which allows more time for the unstable mode to grow. We discuss the astronomical implication of these results in Section 4.2.

4. Discussion

In this work, we study the drag instability in non-self-gravitating, steady-state 1D C-shocks under particular conditions representative of the condition in turbulent star-forming molecular clouds. In this section, we discuss the possible behaviors of the drag instability in numerically evolving C-shocks (Section 4.1) and in the physical space (i.e., under the existence of self-gravity; Section 4.2) to further explore the practical applications of the drag instability. Because there is currently no direct observational evidence of C-shocks in turbulent clouds (see the references in Section 1), we frame our arguments using numerical C-shocks and/or the typically observed properties of the parent clouds wherein the C-shocks form as general guidance.

We also note that it is currently not clear whether the drag instability can occur in oblique C-shocks (see, e.g., Wardle 1991; Mac Low et al. 1995; Ashmore et al. 2010; CO12), which requires one more dimension than our 1D analysis here. The drag instability can occur in 1D systems because of the ionization and recombination terms in the continuity equation of ions (see Equation (2)). These source terms facilitate the growth of density clumps in 1D via drag in the absence of magneto-acoustic modes and another dimension. In contrast, it has been known that the ionization equilibrium precludes the Wardle instability (a 2D/3D effect) in C-shocks (Wardle 1990; Mac Low & Smith 1997; Stone 1997). Analogously, it is worth noting that as an incompressible mode, the streaming instability (see Section 1) is prohibited in a 1D flow (Youdin & Goodman 2005). We thus restrict our discussions below to 1D systems alone.

4.1. Drag Instability in C-shock Simulations

While the model of the drag instability was developed based on the steady-state profile of C-shocks, it is possible that the drag instability could occur in time-dependent simulations of C-shocks. Conceptually, this could occur when the evolving C-shock system is very close but not exactly equal to the steady-state C-shock structure. If the deviation from the steady-state profile happens to satisfy the unstable mode favored by the drag instability, this local perturbation could evolve and grow with time.

In addition to deriving the structure of a steady-state C-shock, CO12 also numerically obtained the C-shock structure by simulating two colliding flows using the ATHENA code (Stone et al. 2008). Instead of computing two fluids comprising the ions and neutrals, as shown in Equations (1)–(5), CO12 simulated the equations for the neutrals alone under the strong-coupling approximation, that is, $\boldsymbol{f_d} = \boldsymbol{f_L} = (1/4\pi)(\nabla \times \boldsymbol{B}) \times \boldsymbol{B}$. Therefore the two-fluid equations considered in this study can be reduced to the following one-fluid equations for the neutrals (see also, e.g., Mac Low et al. 1995):

$$\frac{\partial \rho_n}{\partial t} + \nabla \cdot (\rho_n \boldsymbol{v_n}) = 0 \qquad (26)$$

$$\rho_n \left[\frac{\partial \boldsymbol{v_n}}{\partial t} + (\boldsymbol{v_n} \cdot \nabla) \boldsymbol{v_n} \right] + \nabla p_n = \frac{1}{4\pi}(\nabla \times \boldsymbol{B}) \times \boldsymbol{B} \qquad (27)$$

$$\frac{\partial \boldsymbol{B}}{\partial t} + \nabla \times (\boldsymbol{B} \times \boldsymbol{v_n})$$

$$= \nabla \times \left\{ \boldsymbol{B} \times \left[\frac{1}{4\pi\gamma\rho_i\rho_n}(\nabla \times \boldsymbol{B}) \times \boldsymbol{B} \right] \right\}. \qquad (28)$$

Note that the momentum equation (Equations (26)) and the mass conservation equation (Equations (27)) for neutrals are identical to that in the ideal MHD limit (see Equations (1) and (3)), but the induction equation (Equations (5)) now has a correction term from the ion–neutral drift (see also Equation (46) in CO12). Although the numerical results of CO12 were consistent with the analytical expectation for the C-shock structure, no instabilities were observed in their simulations. This result contrasts with the result of our linear analysis. We discuss possible explanations below.

Because the drag instability is derived from the two-fluid model in this study, we examine whether the strong-coupling approximation can dismiss the drag instability in the one-fluid

model adopted in Mac Low et al. (1995) and CO12, for example. In the two-fluid model, the drag instability arises from the perturbed drag term $\gamma \rho_i V_d \delta \rho_i / \rho_i$ in the momentum equation for the neutrals (see Equation (17)). In the one-fluid model, this term is replaced by the perturbation of magnetic pressure $-(V_{A,n}^2/B) d\delta B/dx = -ik(V_{A,n}^2/B)\delta B$, which is in turn linked to the perturbation of the diffusion-corrected induction equation (Equation (28)):

$$\Gamma \delta B + ik\delta v_n B \approx \frac{V_{A,n}^2}{\gamma \rho_i}\left(\frac{d^2\delta B}{dx^2} - \frac{1}{\rho_n}\frac{d\delta\rho_n}{dx}\frac{dB}{dx}\right)$$
$$= -k^2 \frac{V_{A,n}^2}{\gamma \rho_i}\delta B + ikV_d \frac{\delta\rho_n}{\rho_n}B. \qquad (29)$$

Note that we have adopted the WKBJ approximation but still retained the term with dB/dx due to a large V_d ($\propto dB/dx$) for our interest. The two terms from the right-hand side of Equation (29) arise from the perturbation of the ambipolar diffusion. The first term is the typical diffusion term $k^2 D_{\mathrm{ambi}}$ with the ambipolar diffusivity $D_{\mathrm{ambi}} \equiv V_{A,n}^2/(\gamma \rho_i)$. Rearranging the above equation, we find

$$-ikV_{A,n}^2 \frac{\delta B}{B} \approx \gamma \rho_i V_d \frac{\delta\rho_n}{\rho_n} - \gamma \rho_i \delta v_n + i\frac{1}{k}\Gamma\gamma\rho_i\frac{\delta B}{B}, \qquad (30)$$

where the first term on the right-hand side (i.e., the last term on the right-hand side of Equation (29)) is the term required for the drag instability in the two-fluid model. This suggests that the drag instability can occur in the strong-coupling limit.

Indeed, the ion–neutral drift in some of the simulated C-shocks may not be sufficiently strong to either initiate the drag instability (models Fig4CO12 and Fig5CO12 in Table 2) or generate appreciable growth without an initial perturbation from the background structure (i.e., the steady-state solution). Another possible factor of the missing instability is numerical resolution. The spacial resolution adopted in CO12's 1D simulations is 0.01 pc, which could be too coarse to resolve the drag instability. In fact, as shown in Figure 6, the wavenumber k corresponds to the unstable mode in our fiducial model is $\gtrsim 500$ pc^{-1} within the C-shock, which suggests that the physical scale of the growing perturbation could be smaller than 0.002 pc.

We further note that the drag instability has not been reported in most of the previous studies investigating the 1D C-shock structure (e.g., Smith & Mac Low 1997; Chieze et al. 1998; Ciolek & Roberge 2002; van Loo et al. 2009). Smith & Mac Low (1997) adopted the so-called frozen-in condition (e.g., Wardle 1990) assuming ion conservation. This means that ionizations and recombinations are neglected, and the ion number density through the C-shock is purely determined by the compression of the magnetic field via the ion conservation equation and the induction equation. Because the dependence of the ion density on the neutral density is essential for the drag instability to occur, it is not surprising that the drag instability was suppressed in their simulations. For works that included microphysics and/or the chemistry of the C-shock system (e.g., Chieze et al. 1998; Ciolek & Roberge 2002; van Loo et al. 2009), the ionization and recombination processes became more complicated and could affect the timescale on which the drag instability grew. We also note that the increased gas temperature from shock compression (up to $\sim 10^2$–10^3 K) may

completely prevent the drag instability (which is derived using isothermal equation of state) in these simulations.

4.2. The Significance of the Drag Instability in Astronomical Systems

In this work, we study the drag instability in C-shocks with conditions that can arise from clump–clump collisions or cloud-scale supersonic turbulent flows in typical star-forming regions. One of the most tantalizing questions for shocks in this context is whether a shock instability can lead to fragmentation that is subject to gravitational collapse and eventually induce star formation. However, our analysis here focuses on the behavior of the drag instability within the steady-state profiles of C-shocks, which is linear and non-self-gravitating. These linear analyses are therefore not applicable to directly address this issue and predict any nonlinear outcomes.

Nonetheless, the linear theory could still provide indications on the possible consequence of the instability. The values of the MTG listed in Table 2 indicate that under preferred circumstances, a small perturbation from the steady-state solution could lead to large ($\gtrsim 100\times$) growth. Based on the parameter study, the most favorable condition for drag instability to grow significantly is in strong shocks (high inflow velocities; $v_0 \gtrsim 5$ km s^{-1}). This condition is consistent with the typical environment in giant molecular clouds or molecular cloud complexes (velocity dispersion $\sigma_v \sim 1$–10 km s^{-1}; see recent observations in, e.g., Heyer et al. 2009; Miura et al. 2012; Evans et al. 2014; García et al. 2014; Nguyen-Luong et al. 2016). The total growth induced by the drag instability can also be further enhanced by efficient ambipolar diffusion, i.e., weak-coupling between neutrals and ions, and/or relatively low ionization fractions ($n_i/n_n \lesssim 10^{-7}$). Because the efficiency of nonideal MHD diffusivity is highly dependent on chemical composition and microscopic physical processes, this condition could be typical in some molecular clouds permitted by dust grain properties, e.g., regions with larger grains (Nishi et al. 1991; Nakano et al. 2002). Still, we note that these conditions potentially favored by the drag instability to develop gravitationally unstable structures were derived following the guidance from the 1D linear analysis, and thus may not be applicable to more complex systems.

In addition, we investigate the perturbation amplitude induced by the drag instability obtained from our eigenvalue problem (see also, e.g., Equation (16)), which is illustrated in Figure 8. Because the amplitude ratio between any two of the perturbations (density, velocity, or magnetic field) remains the same in the linear regime as the unstable mode grows, we plot the relative amplitude of the perturbations in ρ_n, v_n, ρ_i, and v_i normalized by the perturbation in B. Figure 8 shows these perturbations for the growing mode within the C-shock in model V06, which has a moderate MTG in our parameter study (see Table 2). It is evident from the figure that the density perturbations ($\delta\rho_n/\rho_n$, $\delta\rho_i/\rho_i$) are much larger than both the velocity and magnetic field perturbations ($\delta v_n/V_n$, $\delta v_i/V_i$, $\delta B/B$) everywhere in the shock. Similar results are found in other models, which implies that as the perturbations grow due to the drag instability, the density perturbation would reach the nonlinear phase faster than other perturbations. As a result, the density perturbation driven by the drag instability is dynamically significant, and these unstable density enhancements induced by the growing wave mode within C-shocks could become gravitationally important in turbulent molecular
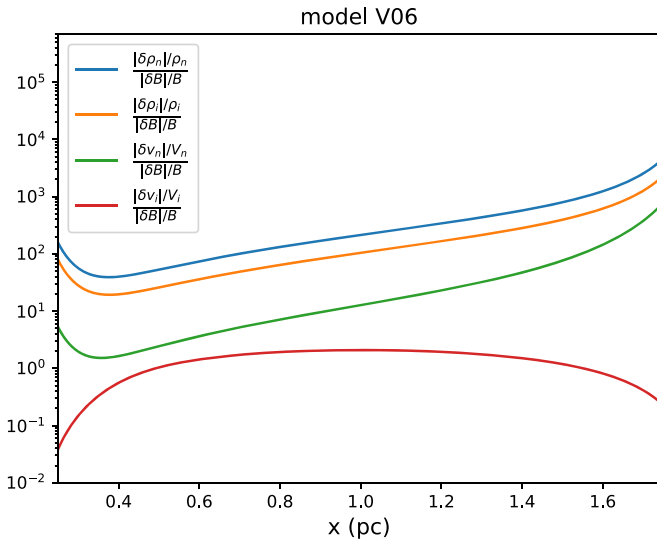
Figure 8. Relative amplitudes of density and velocity perturbations of neutrals and ions (normalized by the magnetic field perturbation) along the C-shock for the growing mode in model V06 (see Table 2 for the model parameters). The density perturbations of both neutrals and ions are much larger than the perturbation in velocities and magnetic field, indicating that the density enhancement induced by the drag instability is dynamically important.

clouds. Further examinations in numerical simulations will help clarify in which scenario the drag instability would become effective during the star-forming process.

5. Summary

Based on the background state of steady C-shocks derived by CO12, we conduct a WKBJ analysis and confirm the postulation of GLV that the drag instability in the ISM can occur in a 1D isothermal C-shock where the ion–neutral drift motion is sufficiently high as a result of the compressed magnetic fields within the smooth shock transition. We first focus on a fiducial case for a C-shock model to study the dispersion relation for the drag instability inside the C-shock. The dispersion relations in the postshock region are also investigated, which reveal all decaying modes associated with ion–neutral collisions, recombination, ambiopler diffusion, and thermal effect. We then solve the linear equations for the exact eigenfrequencies and wavenumber of eigenmodes and identify their physics based on the dispersion relations for growing and decaying modes throughout the C-shock. In our fiducial case, we find that the growing wave driven by the drag instability propagates downstream and subsequently decays by the slow thermal effect associated with neutral-ion collisions in the postshock region.

Because the unstable wave has a considerably higher propagation rate than the local growth rate, the mode with the MTG can be identified as it travels across the entire shock width before it is damped in the postshock region. In addition to the analysis performed with the fiducial model, we also conduct a parameter study to compute the MTG in numerous C-shock models corresponding to the turbulent environment in typical star-forming regions with various preshock parameters n_0, v_0, B_0, and χ_{i0}. We find that the MTG increases with increasing n_0 and v_0, but decreases with increasing B_0 and χ_{i0}. In most cases, the MTG is typically around 10–30 times larger than the initial perturbation for a modest shock, thus requiring the finite amplitude of the initial perturbation to grow to a

nonlinear regime. The drag instability hardly occurs in a weak shock with a shock speed $v_0 = 1 \, \mathrm{km \, s^{-1}}$. Nevertheless, the MTG can become as large as a few hundred for a strong shock with a v_0 value of $\gtrsim 8 \, \mathrm{km \, s^{-1}}$ in our parameter studies.

We leave the numerical investigation of the topics discussed in the previous section for future work. We have also restricted our analysis of the drag instability to a 1D C-shock with a transverse magnetic field for simplicity, which means that the magnetic fields cannot be bent. It will be interesting to extend the work to 2D to study the effect of magnetic tension on the drag instability. A 2D study, both analytically and numerically, will also allow for the investigation of the drag instability in oblique C-shocks following the discussions in Chen & Ostriker (2014). In any case, the analytic solutions of the growth rate and wavenumber in our eigenvalue problem presented in this paper have provided useful information for probing and characterizing the drag instability in simulated time-dependent C-shocks.

ORCID iDs

Pin-Gao Gu ⬤ https://orcid.org/0000-0002-5067-4017
Che-Yu Chen ⬤ https://orcid.org/0000-0002-9209-7916

References

Ashmore, I., van Loo, S., Caselli, P., et al. 2010, A&A, 511, A41
Bai, X.-N., & Stone, J. M. 2011, ApJ, 736, 144
Ballesteros-Paredes, J., Klessen, R. S., Mac Low, M.-M., et al. 2007, in Protostars and Planets V, ed. B. Reipurth et al. (Tucson, AZ: Univ. Arizona Press), 63
Chen, C.-Y, & Ostriker, E. 2012, ApJ, 744, 124
Chen, C.-Y, & Ostriker, E. 2014, ApJ, 785, 69
Chieze, J.-P., Pineau des Forets, G., & Flower, D. R. 1998, MNRAS, 295, 672
Ciolek, G. E., & Roberge, W. G. 2002, ApJ, 567, 947
Crutcher, R. M. 2012, ARA&A, 50, 29
Dalgarno, A. 2006, PNAS, 103, 12269
Dapp, W. B., Basu, S., & Kunz, M. W. 2012, A&A, 541, A35
Draine, B. T. 1980, ApJ, 241, 1021
Draine, B. T., & McKee, C. F. 1993, ARA&A, 31, 373
Draine, B. T., Roberge, W. G., & Dalgarno, A. 1983, ApJ, 264, 485
Evans, N. J., Heiderman, A., & Vutisalchavakul, N. 2014, ApJ, 782, 114
Federrath, C., Sur, S., Schleicher, D. R. G., et al. 2011, ApJ, 731, 62
Fiedler, R. A., & Mouschovias, T. C. 1992, ApJ, 391, 199
Fiedler, R. A., & Mouschovias, T. C. 1993, ApJ, 415, 680
Flower, D. R., & Pineau Des Forêts, G. 1998, MNRAS, 297, 1182
Flower, D. R., & Pineau Des Forêts, G. 2010, MNRAS, 406, 1745
Fukui, Y., & Kawamura, A. 2010, ARA&A, 48, 547
García, P., Bronfman, L., Nyman, L.-Å., et al. 2014, ApJS, 212, 2
Gressel, O., Turner, N. J., Nelson, R. P., et al. 2015, ApJ, 801, 84
Gu, P.-G., Lin, D. N. C., & Vishniac, E. T. 2004, Ap&SS, 292, 261
Guillet, V., Pineau Des Forêts, G., & Jones, A. P. 2011, A&A, 527, A123
Gusdorf, A., Cabrit, S., Flower, D. R., et al. 2008, A&A, 482, 809
Hennebelle, P., Commerçon, B., Chabrier, G., et al. 2016, ApJL, 830, L8
Heyer, M., Krawczyk, C., Duval, J., et al. 2009, ApJ, 699, 1092
Hezareh, T., Csengeri, T., Houde, M., et al. 2014, MNRAS, 438, 663
Hezareh, T., Houde, M., McCoey, C., et al. 2010, ApJ, 720, 603
Indriolo, N., & McCall, B. J. 2012, ApJ, 745, 91

Gu & Chen

Kulsrud, R., & Pearce, W. L. 1969, ApJ, 156, 445
Lam, K. H., Li, Z.-Y., Chen, C.-Y., et al. 2019, MNRAS, 489, 5326
Lehmann, A., & Wardle, M. 2016, MNRAS, 455, 2066
Lesur, G., Kunz, M. W., & Fromang, S. 2014, A&A, 566, A56
Li, H.-B., Goodman, A., Sridharan, T. K., et al. 2014, in Protostars and Planets
    VI, ed. H. Beuther et al. (Tucson, AZ: Univ. Arizona Press), 101
Li, H.-B., & Houde, M. 2008, ApJ, 677, 1151
Li, P. S., McKee, C. F., Klein, R. I., et al. 2008, ApJ, 684, 380
Lizano, S., & Shu, F. H. 1989, ApJ, 342, 834
Mac Low, M.-M., Norman, M. L., Konigl, A., et al. 1995, ApJ, 442, 726
Mac Low, M.-M., & Smith, M. D. 1997, ApJ, 491, 596
Masson, J., Chabrier, G., Hennebelle, P., et al. 2016, A&A, 587, A32
McKee, C. F., Li, P. S., & Klein, R. I. 2010, ApJ, 720, 1612
McKee, C. F., & Ostriker, E. C. 2007, ARA&A, 45, 565
Mellon, R. R., & Li, Z.-Y. 2009, ApJ, 698, 922
Mestel, L., & Spitzer, L. 1956, MNRAS, 116, 503
Miura, R. E., Kohno, K., Tosaki, T., et al. 2012, ApJ, 761, 37
Mouschovias, T. C. 1978, in IAU Coll. 52, Protostars and Planets: Studies of
    Star Formation and of the Origin of the Solar System (Tucson, AZ: Univ.
    Arizona Press), 209
Mouschovias, T. C. 1979, ApJ, 228, 475
Nakano, T., & Nakamura, T. 1978, PASJ, 30, 671
Nakano, T., Nishi, R., & Umebayashi, T. 2002, ApJ, 573, 199
Nguyen-Luong, Q., Nguyen, H. V. V., Motte, F., et al. 2016, ApJ, 833, 23
Nishi, R., Nakano, T., & Umebayashi, T. 1991, ApJ, 368, 181
Oishi, J. S., & Mac Low, M.-M. 2006, ApJ, 638, 281
Ostriker, E. C., Gammie, C. F., & Stone, J. M. 1999, ApJ, 513, 259
Ostriker, E. C., McKee, C. F., & Leroy, A. K. 2010, ApJ, 721, 975
Pineau des Forets, G., Flower, D. R., & Chieze, J.-P. 1997, in IAU Symp. 182,
    Herbig-Haro Flows and the Birth of Stars, ed. B. Reipurth & C. Bertout
    (Dordrecht: Kluwer), 199
Riols, A., & Lesur, G. 2018, A&A, 617, A117
Shu, F. H. 1992, The Physics of Astrophysics, Vol. 2 (Mill Valley, CA: Univ.
    Science Books)
Shu, F. H., Adams, F. C., & Lizano, S. 1987, ARA&A, 25, 23
Smith, M. D., & Mac Low, M.-M. 1997, A&A, 326, 801
Spitzer, L. 1956, Physics of Fully Ionized Gases (New York: Interscience
    Publishers)
Stone, J. 1997, ApJ, 487, 271
Stone, J. M., Gardiner, T. A., Teuben, P., et al. 2008, ApJS, 178, 137
Suriano, S. S., Li, Z.-Y., Krasnopolsky, R., et al. 2018, MNRAS, 477, 1239
Suriano, S. S., Li, Z.-Y., Krasnopolsky, R., et al. 2019, MNRAS, 484, 107
Tang, K. S., Li, H.-B., & Lee, W.-K. 2018, ApJ, 862, 42
Tielens, A. G. G. M. 2005, The Physics and Chemistry of the Interstellar
    Medium (Cambridge: Cambridge Univ. Press)
Valdivia, V., Godard, B., Hennebelle, P., et al. 2017, A&A, 600, A114
van Loo, S., Ashmore, I., Caselli, P., et al. 2009, MNRAS, 395, 319
Vaytet, N., Commerçon, B., Masson, J., et al. 2018, A&A, 615, A5
Wardle, M. 1990, MNRAS, 246, 98
Wardle, M. 1991, MNRAS, 251, 119
Xu, D., & Li, D. 2016, ApJ, 833, 90
Yen, H.-W., Zhao, B., Koch, P. M., et al. 2018, A&A, 615, A58
Youdin, A., & Goodman, J. 2005, ApJ, 620, 459
Zweibel, E. G. 1998, ApJ, 499, 746